

**1 Size-differentiated Export Flux in Different Dynamical  
2 Regimes in the Ocean**

**3 M. Dever<sup>1</sup>, D. Nicholson<sup>1</sup>, M. M. Omand<sup>2</sup>, and A. Mahadevan<sup>1</sup>**

**4** <sup>1</sup>Woods Hole Oceanographic Institution, Woods Hole, MA 02543, USA

**5** <sup>2</sup>Graduate School of Oceanography, University of Rhode Island, Narragansett, Rhode Island, USA

**6 Key Points:**

- 7** • Submesoscale dynamics enhance the contribution of slow-sinking particles to  
**8** POC export, especially for steep particle size-spectrum slopes  
**9** • Remineralization processes intensify the role of slow-sinking particles, to the  
**10** point where these particle sometime dominate POC export

11 **Abstract**

12 Export of Particulate Organic Carbon (POC) is mainly driven by gravitational sinking.  
 13 Thus, traditionally, it is thought that larger, faster-sinking particles make up  
 14 most of the POC export flux. However, this need not be the case for particles whose  
 15 sinking speeds are comparable to the vertical velocities of a dynamic flow field that can  
 16 influence the descent rate of particles. Particles with different settling speeds are re-  
 17 leased in two process-oriented model simulations of an upper ocean eddying flow in the  
 18 Northeast Pacific to evaluate the impact of (1) ocean dynamics on the respective con-  
 19 tribution of the different sinking-velocity classes to POC export, and (2) the particle  
 20 number size-spectrum slope. The analysis reveals that the leading export mechanism  
 21 changes from gravitationally-driven to advectively-driven as submesoscale dynamics  
 22 become more active in the region. The vertical velocity associated with submesoscale  
 23 dynamics enhances the contribution of slower-sinking particles to POC export flux  
 24 by a factor ranging from 3 to 10, especially where the relative abundance of small  
 25 particles is large, (i.e., steep particle size-spectrum slope). Remineralization generally  
 26 decreases the total amount of biomass exported, but its impact is weaker in dynamical  
 27 regimes where submesoscale dynamics are present and export is advectively-driven.  
 28 In an advectively-driven export regime, remineralization processes counter-intuitively  
 29 enhance the role of slower-sinking particles to the point where these slower-sinking ve-  
 30 locity classes dominate the export, therefore challenging the traditional paradigm for  
 31 POC export. This study demonstrates that slow-sinking particles can be a significant  
 32 contribution, and at times, even dominate the export flux.

33 **1 Introduction**

34 Photosynthesis in the sunlit upper ocean and the production of Particulate Or-  
 35 ganic Carbon (POC) takes up dissolved inorganic carbon and facilitates the uptake  
 36 of CO<sub>2</sub> from the atmosphere. The sinking of POC exports organic carbon from the  
 37 upper ocean to the interior, leading to the sequestration of carbon (?, ?) on timescales  
 38 ranging from days to years depending on the sinking depth and circulation. Despite  
 39 progress on sampling and viewing particles in the ocean, direct measurements of par-  
 40 ticles sinking velocities are difficult to obtain, and often inferred from key parameters  
 41 such as particle type, size, and density (?, ?, ?).

42 Traditionally, POC export is thought to occur through gravitational sinking and  
 43 one-dimensional models have been used to describe the sinking POC flux with depth  
 44 (?, ?, ?, ?, ?). Particles produced through primary and secondary production in  
 45 the surface layer that are relatively large and fast sinking tend to sink out of the  
 46 upper surface layer on timescales shorter than the timescale on which the particles  
 47 get remineralized. It is reasonable to treat POC export as sinking-dominated if the  
 48 vertical advective velocities in the ocean are weaker than the velocities associated with  
 49 gravitational sinking. However, Particulate Organic Matter (POM) has a wide range  
 50 of particle shape, size and type, that result in particle sinking velocities ranging from  
 51 practically zero, to several hundreds of meters per day (?, ?, ?). The size spectrum,  
 52 or number distribution of particle sizes, is usually characterized by a power law with  
 53 the power ranging between -2 and -4, for which the abundance of small particles is  
 54  $\mathcal{O}(10^4 - 10^8)$  greater than large particles (?, ?, ?). The biomass size spectrum, which  
 55 indicates the distribution of biomass vs. particle size, tends to be flatter and variable  
 56 in shape (?, ?) compared to the particle number spectrum, because the volume (and  
 57 mass) of a particle scales with its linear size raised to a power that exceeds 1 (and  
 58 typically varies between 2 and 3 depending on shape and porosity). Importantly, it  
 59 means that a significant fraction of the particulate biomass is in the small size fraction  
 60 (?, ?). Even though the sinking velocity  $w_s$  of particles does not perfectly relate to  
 61 particle size  $l$ , it is fair to assume that  $w_s \sim l^n$  (with  $n = 2$  according to Stokes law,  
 62 and  $1 < n < 2$  for complex particle shapes). Due to this, as well as the fact that

63 particles of organic matter are not very much greater in their densities than seawater,  
 64 a significant fraction of the biomass sinks very slowly (at velocities less than tens of  
 65 meters per day). When the gravitational sinking velocity of particles is comparable  
 66 to (or smaller than) the vertical velocities in the flow field, the dynamics of the flow  
 67 field can impact the trajectories and fate of the POC. Thus, depending on the flow  
 68 dynamics, and the fraction of slow-sinking particulate biomass, the sinking of organic  
 69 matter can be affected by the fluid flow in the ocean.

70 Recent studies have shown that ocean dynamics can play a role in driving the  
 71 transport of carbon from the euphotic layer to the ocean interior. For example, en-  
 72 hanced vertical velocities along the edge of a mesoscale eddy led to a funneling of par-  
 73 ticles along the eddy's periphery (?, ?, ?) and in mesoscale features in the California  
 74 current (?, ?). ? (?) found that submesoscale mixed layer eddies, while contributing  
 75 to the restratification of a frontal zone, were subducting a large amount of non-sinking  
 76 POC from the surface productive layer during the onset of the Spring bloom in the  
 77 subpolar North Atlantic. Advectionally subducting plumes or filaments of high oxygen,  
 78 chlorophyll and small POC (evidenced through backscatter) were detected from a suite  
 79 of gliders during the North Atlantic Bloom experiment (Alkire et al., 2012). Using  
 80 model simulations to capture the process of eddy-driven subduction, ? (?) estimated  
 81 the downward advective flux of non-sinking POC and parameterized it. ? (?) quan-  
 82 tified the flux of fast-sinking particles consisting largely of diatoms from observations  
 83 of optical backscatter. But, these estimates did not account for a range of sinking  
 84 particle velocities. Typically, POM has a wide spectrum of sinking velocities and in  
 85 order to understand its fate and export, we need to consider the biomass distribution  
 86 as a function of the particle sinking velocity spectrum and its interaction with the  
 87 dynamics of the flow field in the ocean.

88 A growing body of literature focusing on submesoscale (1-10 km) dynamics is  
 89 exploring its impact on biogeochemical processes (?, ?, ?). Submesoscale dynamics,  
 90 characterized by Rossby numbers of order 1, typically develop in filaments in areas  
 91 where sharp density fronts exist (?, ?, ?, ?). In this dynamical regime, geostrophic bal-  
 92 ance breaks down and a secondary ageostrophic circulation develops across the front,  
 93 capable of generating large vertical velocities on the order of 100 m/day (?, ?, ?). On  
 94 the denser side of the front, the vorticity is cyclonic and associated with downwelling  
 95 velocities, while anticyclonic vorticity and upwelling is expected on the lighter side  
 96 of the front. The distribution of relative vorticity associated with submesoscale dy-  
 97 namics near the surface exhibits an asymmetry with higher values of positive vorticity  
 98 than negative vorticity (?, ?), leading to more localized and more intense downwelling  
 99 regions, as opposed to weaker and larger scale upwelling regions (?, ?). Enhanced ver-  
 100 tical velocities can aid the supply nutrients to the sunlit layer of the ocean for primary  
 101 production (?, ?, ?) or can significantly increase the export of POC to the ocean in-  
 102 terior through localized downwelling (?, ?, ?, ?, ?). The downwelling velocities  $\mathcal{O}(100$   
 103 m/day) generated at submeso-scales provide a physical mechanism for exporting slow  
 104 sinking or neutrally buoyant particles on timescales shorter than their remineralization  
 105 timescales. If the fraction of biomass associated with such slow sinking velocities is  
 106 significant, submesoscale dynamics can potentially impact the export of POC.

107 We rely on a submesoscale-resolving, non-hydrostatic ocean model to simulate  
 108 the dynamics in the upper few hundred meters of the ocean. The dynamical model is  
 109 coupled with a particle-tracking module to model the advection of particles by fluid  
 110 flow, while neglecting the effects of particle inertia and drag on their advection. In  
 111 addition, the particles sink with a range of sinking velocities (between 0.025–5 m  
 112 day<sup>-1</sup>) that is based on the range of vertical currents modeled in this region. We aim  
 113 to address the transitional regime of the particle sinking velocity spectrum, where both  
 114 advection and sinking speeds have similar order of magnitudes. A similar study with

115 sinking tracers showed the influence of the flow (? , ?), but the use of particles enables  
 116 a characterization of export associated with each sinking class of particles.

117 The model is used to quantify the contribution of slow-sinking particles to carbon  
 118 export, as a function of (1) the dynamics of the flow field, (2) the slope of the sinking  
 119 velocity spectrum, and (3) the remineralization timescale. Particles in the model  
 120 are prescribed with both a constant and time-varying sinking velocity to mimic a  
 121 remineralizing behavior. Particles are released in two fundamentally different flow  
 122 fields in terms of dynamics based on observed conditions in the Northeast Pacific:  
 123 In the summer, where ocean dynamics are characterized by low Rossby numbers and  
 124 weak vertical advective velocities, and in the winter, where ocean dynamics include  
 125 submesoscale frontal structures and local Rossby numbers  $\mathcal{O}(1)$ . Both simulations  
 126 and the particle-tracking module are described in Section 2. The impact of particles  
 127 characteristics and ocean dynamics on the export of POC is quantified in Section 3,  
 128 and discussed in Section 4. Section 5 summarizes the key conclusions of the study.

## 129 2 Methods

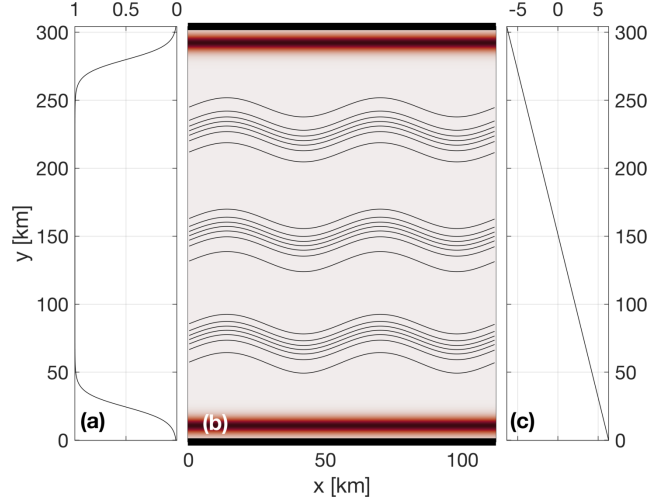
### 130 2.1 Model setup and domain

131 This study uses a non-hydrostatic, three-dimensional, Process Study Ocean Model  
 132 (PSOM; ?, ?, ?) to simulate an eddy field that is representative of the Northeast Pacific  
 133 Ocean. The model is set in a channel configuration with periodic east-west bound-  
 134 aries, and solid boundaries in the south and north. The domain covers 112 km in the  
 135 x-direction, 304 km in the y-direction, and 1000 m in the vertical (Figure 1). The hor-  
 136 izontal resolution is 500 m, while a stretched grid is used in the vertical with 32 levels  
 137 ranging in thickness from 1.25 m near the surface to 70 m at the lowermost level.  
 138 The model is integrated numerically in time and evolves the temperature, salinity,  
 139 free-surface height, pressure, and three-dimensional velocity field from an initial state,  
 140 subject to momentum and buoyancy fluxes applied through the surface boundary.

148 Time-varying wind stress and heat flux are prescribed at the surface boundary.  
 149 Time series are computed from measurements collected at Station Papa and available  
 150 through the Pacific Marine Environmental Laboratory (? , ?). Daily wind stress and net  
 151 heat fluxes are calculated over the period 2007-2016 to produce a year-long climatology.  
 152 A squared low-pass filter with a cut-off frequency of 8.5 days is applied to both time  
 153 series to remove high-frequency variability. In all numerical experiments, simulations  
 154 are run for the first 5 days without any forcing applied to the surface boundary. Surface  
 155 wind stress and heat fluxes are then linearly ramped up between days 5 and 10 of the  
 156 simulation, to reach realistic values at day 10.

157 While the meridional component,  $\tau_y$ , is set to zero, the zonal component of  
 158 the wind stress,  $\tau_x$ , is prescribed at the surface throughout the model domain and  
 159 is tapered at the northern and southern boundaries to avoid excessive Ekman-driven  
 160 upwelling and downwelling (Figure 1a). A restoration timescale is prescribed to contain  
 161 the curl-driven upwelling and downwelling regions generated by the tapering of the  
 162 wind stress, as well as to limit internal wave reflection at the solid boundaries back  
 163 into the domain (Figure 1b). While net surface heat fluxes are homogeneous in the  
 164 zonal direction, a meridional gradient is maintained throughout the simulation. The  
 165 meridional gradient was determined from the North American Regional Reanalysis  
 166 (NARR) product (? , ?), and set to 1/24 W/m<sup>2</sup>/km (Figure 1c).

167 Initial hydrographic conditions are determined from a three-dimensional gridded  
 168 field of temperature and salinity from Argo floats (? , ?, ?). Argo data is averaged  
 169 monthly over the period 2002-2012 and two different months are used to initialize the  
 170 two main numerical experiments for this study: Climatological conditions in April are  
 171 used to initialize the *Papa-summer* experiment, while January climatological condi-



141 **Figure 1.** PSOM model setup. (a) Meridional profile of scaling coefficient that multiplies the  
 142 time-varying zonal wind stress  $\tau_x$  shown in Fig. 3a. The taper at north and south boundaries  
 143 prevents ‘coastal’ up-/down-welling being entirely concentrated in the boundary grid cell. (b)  
 144 Restoration factor (color shading) used to dampen internal wave reflection at boundaries as well  
 145 as up-/down-welling due to the windstress curl. Surface density contours (black) show the three  
 146 fronts used to initialize the model. (c) Meridional variation of the time-dependent surface heat  
 147 flux (Fig. 3a) prescribed over the domain.

172 tions are used to initialize the *Papa-winter* experiment (Table 1). The north-south  
 173 background density gradient is then intensified into three fronts located at  $y = 75$ ,  
 174  $y = 150$ , and  $y = 225$  km (Figure 1). The amplitude of the density gradient associated  
 175 with the three fronts is determined from the probability distribution function (PDF)  
 176 of the density gradients measured by underwater gliders deployed around Station Papa  
 177 over the period 2008-2010 (? , ? , ?). To reduce model spin-up time, density fronts are  
 178 perturbed by a sinusoidal wave with a wavelength close to the 1st baroclinic defor-  
 179 mation radius ( $\lambda = 66$  km). Similar PSOM configurations were successfully used in  
 180 previous studies (? , ? , ?). The model does not simulate surface waves or boundary  
 181 layer turbulence, but rather, examines the fate of particulate organic matter beneath  
 182 the turbulent surface boundary layer.

183 Two main experiments are conducted using the same configuration of PSOM,  
 184 where only initial conditions and surface forcings are varied: *Papa-summer* aims at  
 185 generating ocean dynamics representing conditions in the Northeast Pacific in the sum-  
 186 mertime. Summer ocean dynamics are characterized by a flow generally in geostrophic  
 187 balance, with relatively weak density gradients and low Rossby numbers ( $Ro \ll 1$ ).  
 188 *Papa-winter* aims at capturing wintertime ocean conditions in the region. A different  
 189 dynamical regime is expected to dominate during wintertime when mixed layers are  
 190 deeper and lateral density gradients enhanced, with sharper density fronts, filament-  
 191 like features and localized Rossby number  $Ro = \mathcal{O}(1)$  over spatial scales  $\mathcal{O}(1 \text{ km})$  (? ,  
 192 ?, ?, ?). The individual characteristics of each of *Papa-summer* and *Papa-winter* are  
 193 detailed below.

### 194 2.1.1 *Papa-summer Model Experiment*

195 In *Papa-summer*, PSOM is initialized based on climatological Argo data in April.  
 196 The magnitude of the density gradient across the front is set to  $3.34 \times 10^{-6} \text{ kg/m}^3/\text{m}$ ,

206      **Table 1.** Summary of the key characteristics of PSOM experiments *Papa-summer* and  
 207      *Papa-winter*.

	<i>Papa-summer</i>	<i>Papa-winter</i>
Time period	April – July	January – March
Spin-up	60 days	50 days
Advective timestep	216 s	108 s
Horizontal diffusivity	$1 \text{ m}^2 \text{ s}^{-1}$	$0.2 \text{ m}^2 \text{ s}^{-1}$
Restoration timescale	3 days	15 days
Zonal wind stress	$0 - +0.16 \text{ N m}^{-2}$	$-0.05 - +0.17 \text{ N m}^{-2}$
Surface heat flux	$-46.8 - +167.5 \text{ W m}^{-2}$	$-57.6 - +15.3 \text{ W m}^{-2}$
Maximum $M^2 (\times 10^{-8})$		
initial	$3.2 \text{ s}^{-2}$	$33.9 \text{ s}^{-2}$
spun-up	$12.0 \text{ s}^{-2}$	$50.0 \text{ s}^{-2}$
Maximum $N^2 (\times 10^{-4})$		
initial	$1.5 \text{ s}^{-2}$	$1.6 \text{ s}^{-2}$
spun-up	$3.1 \text{ s}^{-2}$	$1.1 \text{ s}^{-2}$
Averaged mixed layer depth		
initial	73 m	85 m
spun-up	11 m	93 m

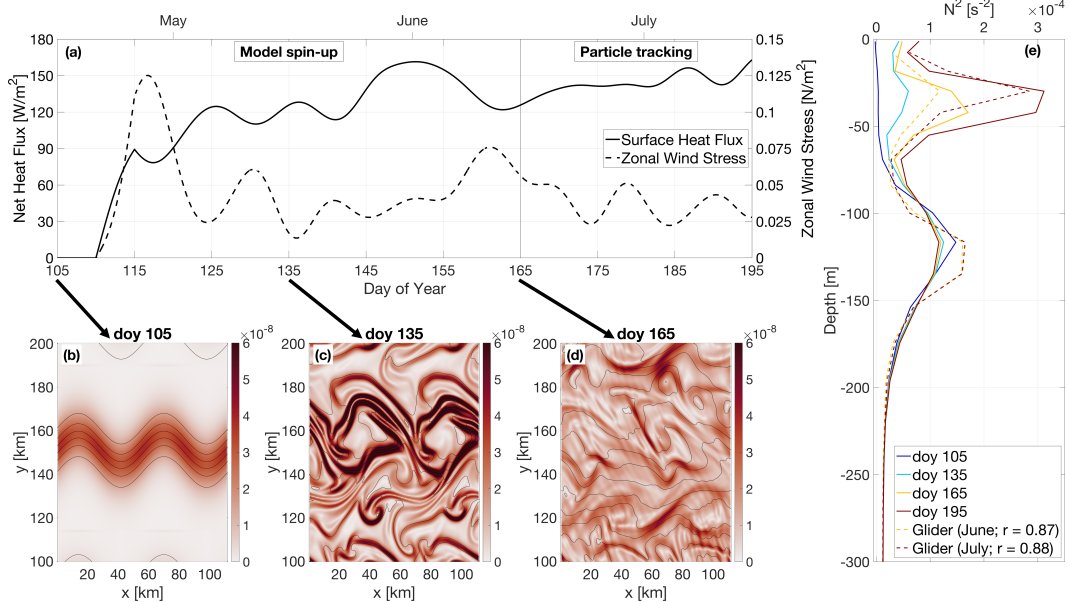
197      which corresponds to the 95<sup>th</sup> percentile of the PDF of density gradients measured  
 198      in April from glider data collected in the region (Figure 2 and Table 1). The model  
 199      is run with a timestep of 216 s and is allowed to spin-up for 60 days, allowing sum-  
 200      mer stratification to develop. The model is then run for 30 additional days, saving  
 201      instantaneous model fields every 3 hours for particle tracking. The month of April  
 202      is chosen for initialization so the experiment would capture the onset of positive net  
 203      heat fluxes, and the summer restratification that ensues in July-August (Figure 2). In  
 204      this region, the summer stratification is associated with large primary productivity,  
 205      particle production, and POC export (e.g., fecal pellets, dead phytoplankter; ?, ?).

### 217      2.1.2 *Papa-winter Model Experiment*

218      In *Papa-winter*, PSOM is initialized based on climatological Argo data in Jan-  
 219      uary. The frontal gradient is set to  $3.54 \times 10^{-5} \text{ kg/m}^3/\text{m}$ , which corresponds to the  
 220      99<sup>th</sup> percentile of the PDF of density gradients measured in January from glider data  
 221      collected in the region (Figure 3 and Table 1). The model is allowed to spin-up for 50  
 222      days allowing for the prescribed fronts to become unstable. To accommodate for the  
 223      larger density gradients and stronger velocities, the advective timestep is shortened to  
 224      108 s and the horizontal diffusivity is lowered to  $0.2 \text{ m}^2/\text{s}$  throughout the experiment.  
 225      The model is run for 30 additional days, saving instantaneous model fields every 1.5  
 226      hours for particle tracking. The month of January is chosen for initialization so the  
 227      experiment would capture the time of year where the mixed layer is the deepest, and  
 228      Rossby number O(1) occur more frequently. The objective is for this experiment to  
 229      contrast *Papa-summer* by capturing the statistics of ocean conditions dominated by  
 230      submesoscale dynamics.

### 239      2.1.3 *Validation*

240      To ensure that PSOM simulations yielded realistic conditions for both *Papa-summer*  
 241      and *Papa-winter*, distributions of horizontal ( $M^2$ ) and vertical ( $N^2$ ) buoyancy gradi-  
 242      ents are compared with glider observations collected over the period 2008-2009 (?, ?).



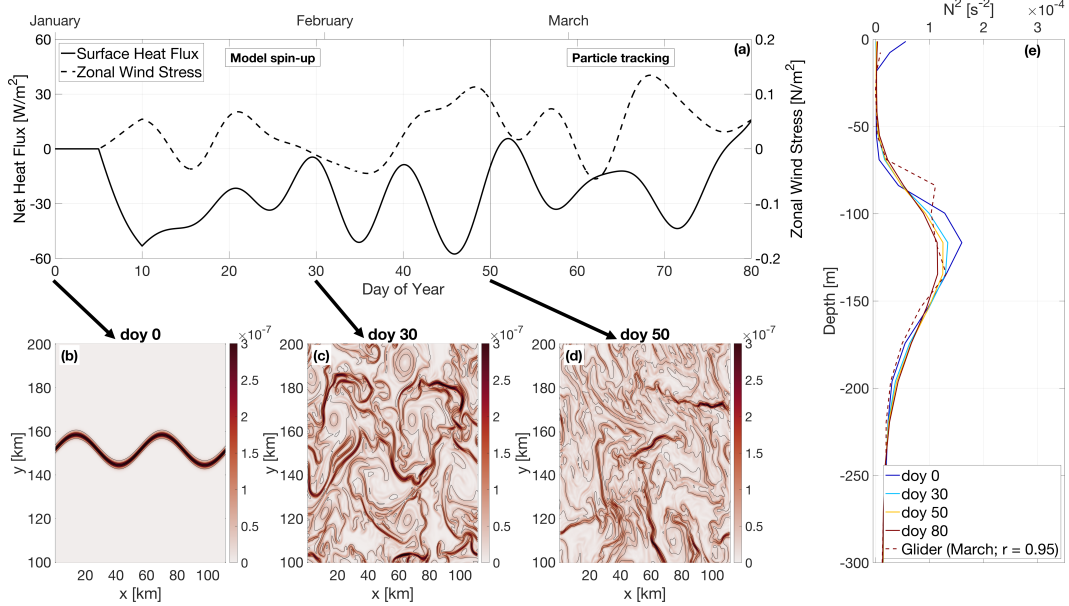
208 **Figure 2.** PSOM configuration for *Papa\_summer*. (a) Time series of net heat fluxes and wind  
 209 stress prescribed at the surface. Notice the positive heat fluxes, as well as downfront winds (i.e.  
 210 eastward) persisting throughout the experiment. (b)-(d) surface horizontal buoyancy gradients  
 211  $M^2 = |\nabla_H b|^2$  (in  $s^{-2}$ ) at day of year (doy) 105, 135, and 165. Black contours show isopycnals (in  
 212 kg/m<sup>3</sup>; CI = 0.01 kg/m<sup>3</sup>). (e) Vertical profile of the buoyancy frequency  $N^2$  at day of year 105,  
 213 135, 165, and 195, showing the development of summer stratification centered at  $z = 30$  m (solid  
 214 lines). Monthly-average vertical stratification obtained from glider profiles collected in June and  
 215 July are superimposed (dashed lines), along with the correlation coefficient between observations  
 216 and model outputs.

243 During this period, underwater gliders sampled in a “bow-tie” pattern centered on  
 244 Station Papa. Gliders sample the water column in a triangular wave pattern, whose  
 245 shape is easily affected by currents, due to the slow moving speed of the glider (~1  
 246 km/hr). It is therefore challenging to associate a specific spatial scale with gradients  
 247 computed between glider profiles, as profile separation distances can be highly vari-  
 248 able through depth and time. To circumvent this issue, horizontal buoyancy gradients  
 249 are computed between each pair of glider profiles available within one branch of the  
 250 bow-tie. Each along-track lateral buoyancy gradient is thus associated with a specific  
 251 separation scale and a timestamp. Glider-based density gradients can be affected by  
 252 internal waves. To filter the impact of internal waves on the PDF of horizontal buo-  
 253 yancy gradients, only gradients computed at a scale of twice the Rossby radius  $\pm 1$  km  
 254 are considered. Rossby radii are estimated from the glider data and are  $\sim 8$  km in  
 255 winter and  $\sim 20$  km in summer.

## 256 2.2 Particle Tracking Experiments

### 257 2.2.1 Particle Advection Scheme

To quantify the impact of submesoscale dynamics on the export of Particulate Organic Matter (POC), Lagrangian particle trajectories are computed using the same scheme as in “TRACMASS” (?, ?) with the flow fields from the two experiments described above. The three-dimensional, non-divergent velocity components from the



231 **Figure 3.** PSOM configuration for *Papa\_winter*. (a) time series of net heat fluxes and wind  
 232 stress prescribed at the surface. Notice the mostly negative heat fluxes, as well as alternating  
 233 zonal wind direction. (b)-(d) surface horizontal buoyancy gradients  $M^2 = |\nabla_H b|^2$  (in  $s^{-2}$ ) at day  
 234 of year (doy) 0, 30, and 50. Black contours show isopycnals (in  $kg/m^3$ ; CI =  $0.01\ kg/m^3$ ). (e)  
 235 Vertical profile of the buoyancy frequency  $N^2$  at doy 0, 30, 50, and 80, showing the persistence  
 236 of the halocline between  $z = 80$  and  $z = 180$  m throughout the experiment (solid lines). Monthly-  
 237 average vertical stratification obtained from glider profiles collected in March is superimposed  
 238 (dashed line), along with the correlation coefficient between observations and model outputs.

faces of each “C” grid cell are linearly interpolated onto the particle’s position within the grid cell. For example, the eastward (along the x-axis) velocity of a particle is given by

$$u(x) = u_{i-1} + \frac{(x - x_{i-1})}{(x_i - x_{i-1})}(u_i - u_{i-1}), \quad (1)$$

where the subscripts  $i - 1$  and  $i$  denote the western and eastern walls of the grid cell where the particle is located, respectively. This can be re-written as

$$\frac{\partial x}{\partial t} + \beta x + \delta = 0, \quad (2)$$

where  $\beta = (u_i - u_{i-1})/\Delta x$  and  $\delta = -u_{i-1} - \beta x_{i-1}$  (?). This differential equation can be solved analytically for  $\beta \neq 0$  as

$$x_{t_1} = \left( x_0 + \frac{\delta}{\beta} \right) \exp^{-\beta(t_1 - t_0)} - \frac{\delta}{\beta} \quad (3)$$

The time it will take for the particle to reach the eastern or western face of the grid cell can be computed by taking  $x_{t_1} = x_i$  or  $x_{t_1} = x_{i-1}$ , respectively, and solving for  $t_1$ . For each advective timestep, the times required for the particle to reach any of the 6 walls of the grid cell are computed using (3). If any of those times is shorter than the advective timestep, the particle is advected until it reaches the cell wall. Then the flow field in the adjacent grid cell is considered and the particle is advected over the remaining time.

265      **2.2.2 Particle Seeding**

266      For all particle-tracking experiments, a single particle seeding event is prescribed.  
 267      In the horizontal, particles are seeded every 250 m over the entire domain in the x-  
 268      direction, and for  $100 < y < 200$  km in the y-direction. The seeding is centered over  
 269      the mean position of the central front (see Figure 2) and is therefore not affected by  
 270      undesired effects created by the solid north-south solid boundaries. In the vertical,  
 271      particles are seeded every 1 m between 75 and 85 m. This depth range is chosen as it  
 272      corresponds to the average euphotic depth at Station Papa, defined by the 1% light  
 273      level. Particle seeding is located at the base of the euphotic layer where biological  
 274      processes not captured by the particles (e.g., grazing, repackaging, aggregation, etc.)  
 275      are not as active (? , ?). The euphotic depth was computed for the months of February  
 276      and June over the period 2007-2016 from profiles of Photosynthetically Active Radi-  
 277      ration (PAR) collected at Station Papa as part of the long-term monitoring of Line P  
 278      executed by the Department of Fisheries and Ocean Canada<sup>1</sup>. The average euphotic  
 279      depth computed for both of these months is around 80 m, which agrees with previously  
 280      established estimates of the euphotic depth (? , ? , ?).

281      In each particle-tracking experiment, three different classes of particles are re-  
 282      leased. Each particle class is characterized by a different sinking velocity: 0.025, 1,  
 283      and 5 m/day. In this study, these particle classes are referred to as slow-, intermediate-,  
 284      and fast-sinking particles. This characterization is not based on the absolute value of  
 285      the sinking rate, but rather on the ratio with vertical currents in the study region. The  
 286      slowest-sinking class is essentially selected to represent non-sinking particles: based on  
 287      the setup of our experiments, the slowest-sinking particles would take 400 days to sink  
 288      10 m through gravitational sinking, a timescale much greater than commonly observed  
 289      remineralization timescales. While 5 m/day remains a relatively slow sinking rate, this  
 290      “fastest-sinking” velocity is chosen as an end-member velocity class of particle, based  
 291      on the PDF of vertical velocities in the model. At any given time, at least 85% of  
 292      the model vertical velocity is weaker than 5 m/day. The results presented for the 5  
 293      m/day sinking class can therefore be theoretically extrapolated to any class with a  
 294      higher sinking velocity.

295      The advective timestep for particles is set to 1.5 hours. The flow field is linearly  
 296      interpolated in time between model outputs, justifying the higher temporal resolution  
 297      used for particle tracking in *Papa\_winter*. Particle positions are saved every 3 hours,  
 298      along with key model variables interpolated onto the particle positions (e.g., density,  
 299      vorticity). Particles are tracked for four weeks (28 days). Each particle-tracking ex-  
 300      periment contains 1,971,717 particles per sinking-velocity class, for a total of 9,858,585  
 301      particles. Particles located deeper than the maximum winter mixed layer (i.e., 100 m;  
 302      ?, ?, ?) are considered exported, as they will likely not be re-entrained into the mixed  
 303      layer.

304      **2.2.3 Density and Biomass Spectra**

To quantify vertical export fluxes, both the distribution of the number of particles and the associated biomass can be modeled based on two main variables: the particles’ radii and the rate at which the number of particles changes with respect to the size. The particle number is modeled using a power-law function as a function of size that is driven by the parameter  $\xi$ . This slope  $\xi$  of the size spectrum of particles (also known as the Junge slope; ?, ?) is the slope of the log-log curve of particle number  $N$  vs.

---

<sup>1</sup> <https://www.waterproperties.ca/linep/index.php>

particle radius  $r$ , where

$$N(r) = N_0 \left( \frac{r}{r_0} \right)^{-\xi}. \quad (4)$$

Here,  $N_0$  and  $r_0$  represent a reference particle number and radius, chosen arbitrarily. Typical values for  $\xi$  derived from both in-situ observations and satellite data have been reported to range from 3 to 6 (?, ?, ?). For small particles ( $<400 \mu\text{m}$ ) and relatively low temperature ( $<15^\circ\text{C}$ ), it has been shown that the relationship between particle radius  $r$  and sinking velocity  $w_s$  exhibits a range of variation and is difficult to determine empirically. Nevertheless, Stokes' law, where  $w_s \propto r^2$ , is often used as a lower-bound sinking velocity estimate (?, ?).

Assuming a Stokes-like relationship, we can construct based on (4) a particle sinking velocity spectrum  $N(w_s)$ , as a function of the Junge slope  $\xi$ :

$$N(w_s) = N_0 \left( \frac{w_s}{w_{s_0}} \right)^{-\xi/2}, \quad (5)$$

where  $w_{s_0}$  is the sinking speed of particles with radius  $r_0$ . For a specific slope and sinking-velocity class, an equivalent number of particles per simulated particle can be computed using (5) (See Figure 4). For example, using the largest sinking velocity class as a reference (i.e.,  $w_{s_0} = 5 \text{ m/day}$  and  $N_0 = 1,971,717$ ), and a spectral slope  $\xi = 4$ , each simulated particle with a sinking velocity of  $0.025 \text{ m/day}$  in fact represents 40,000 particles (Figure 4).

The relative biomass of a particle in a specific sinking-velocity class,  $B_p(w_s)$  can be estimated if the biomass is assumed to scale with the particle's volume. The relative biomass of one particle in a sinking-velocity class  $w_s$  can therefore be computed as

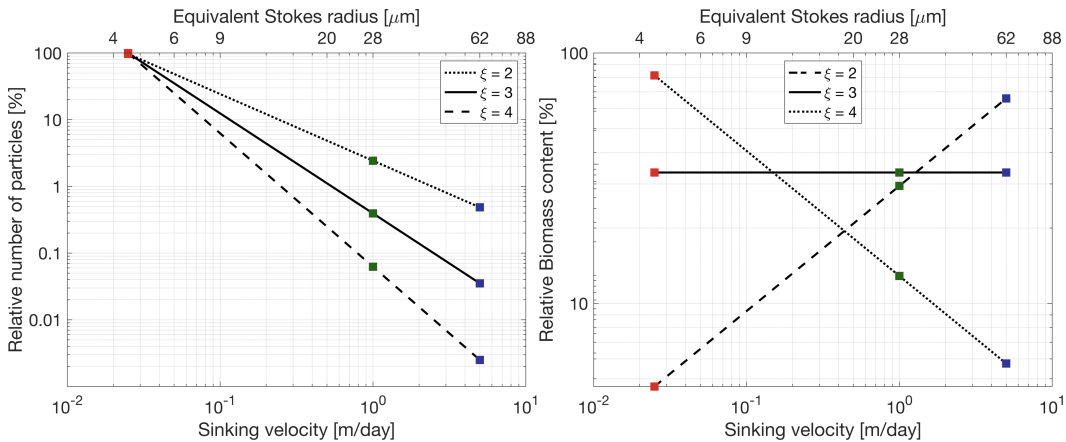


**Figure 4.** Relative number of particles (left) and biomass (right) as a function of sinking velocity  $w_s$ . Sinking velocity spectrum are shown for three different Junge slope  $\xi$ : 2 (dotted), 3 (solid), and 2 (dashed). Colored squares indicate the sinking velocities of the three particle classes modeled: 0.025 m/day (red), 1 m/day (green), and 5 m/day (blue).

$$B_p(w_s) = B_p(w_{s_0}) \left( \frac{w_s}{w_{s_0}} \right)^{3/2} \quad (6)$$

where  $B_p(w_{s_0})$  is the biomass of a particle in the sinking velocity class  $w_{s_0}$ . The total biomass associated with one simulated particle can be obtained by scaling (6) by the

ratio  $N(w_s)/N_0$ :

$$B(w_s) = B_0 \left( \frac{w_s}{w_{s_0}} \right)^{3/2} \frac{N(w_s)}{N_0} \quad (7)$$

where  $B_0 = B_p(w_{s_0})$ . Combining (5) and (7) yields an expression relating the biomass associated with a simulated particle for a specific sinking-velocity class and the spectral slope (Figure 4):

$$B(w_s) = B_0 \left( \frac{w_s}{w_{s_0}} \right)^{\frac{3-\xi}{2}}. \quad (8)$$

Using the same example as before where  $\xi = 4$ , if the amount of biomass associated with one simulated particle in the 5 m/day sinking-velocity class is taken as  $B_0 = 1$ , then one simulated particle sinking at 0.025 m/day contains 14.14 units of biomass and a single particle contains  $14.14/40,000 = 3.5 \times 10^{-4}$  units of biomass (see Figure 4). This normalized formulation of particle number and biomass (see Equations (5) and (8)) has the advantage that the impact of spectral slope on the relative export of biomass can be quantified without needing a large number of particle-tracking experiments, where the number of seeded particles would vary to account for the different spectral slopes. For the purpose of this study, only the relative amount of biomass is relevant. For simplicity, we define a normalized biomass unit for  $\xi = 3$  as  $B_0 = 1$ . The values taken by  $B_0$  for other Junge slopes  $\xi$  are computed under the condition that the total amount of biomass is kept constant (Figure 4b).

#### 2.2.4 Particle Remineralization Scheme

Remineralization of particles as they sink through the water column impacts the amount of biomass exported. Slow-sinking particles generally contain less biomass and spend more time in the mixed layer, which means that they are remineralized at a shallower depth than faster sinking particles. Remineralization processes are complex, species-dependent, and generally not well-understood. In the absence of a consensus on a general functional form of particle remineralization, we rely on an idealized relationship which assumes that the biomass content of a particle decreases in time proportionally to the particle volume. Remineralization is thus modeled as an exponential decrease of biomass with time at a rate  $k$  (?, ?, ?)

$$B(t) = B^0 \exp(-kt), \quad (9)$$

where  $B^0$  denotes the biomass content at  $t = 0$  days, and the remineralization rate is taken to be  $k = 0.13 \text{ day}^{-1}$  in this study (?, ?). This remineralization rate is independent of particle sinking velocity, and seems to lie within the range of other estimates (?, ?, ?, ?). The change in biomass with time is in turn expected to affect the sinking velocity of the particle. Given that  $B \propto w^{3/2}$  (see Equation (6)), particles in all sinking-velocity classes undergo a decay in sinking speed according to

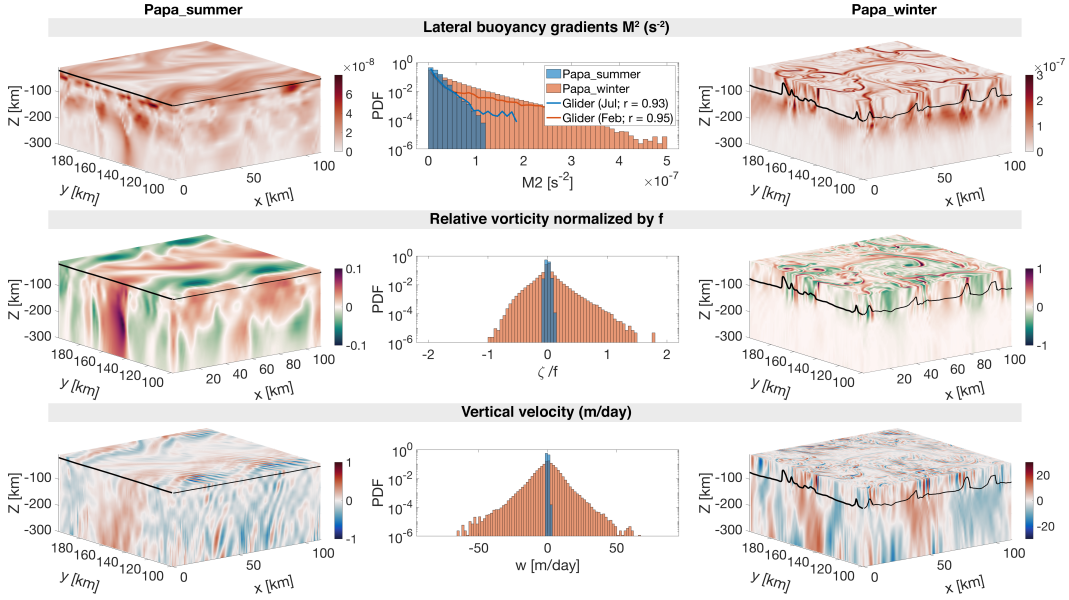
$$w_s(t) = w_s^0 \exp\left(-\frac{2kt}{3}\right), \quad (10)$$

where  $w_s^0$  is the initial sinking velocity at  $t = 0$  days. In this study, the impact of remineralization is thus considered through the implementation of a time-dependent sinking velocity (Equation 10). While particles classes are classified based on their initial sinking-velocity, it is worth noting that over the length of the particle-tracking experiments that include remineralization (28 days), particle sinking speeds slow down to 10% of their initial velocity.

### 3 Results

#### 3.1 Seasonally varying dynamical regimes

Two model experiments are designed to capture different dynamical conditions observed in the Northeast Pacific Ocean in summer and winter. *Papa\_summer* is ini-



365 **Figure 5.** Snapshots of  $M^2$  (top),  $\zeta/f$  (middle), and  $w$  (bottom) half-way through the particle tracking experiment for *Papa\_summer* (left) and *Papa\_winter* (right), with the Mixed Layer Depth indicated by the solid black line. The corresponding Probability Distribution Functions (PDFs) are shown in the center for both *Papa\_summer* (blue) and *Papa\_winter* (red). Note the different colorbars used for *Papa\_summer* and *Papa\_winter*. Histograms of  $M^2$  computed from glider data at Station Papa in February (blue line) and July (red line) are superimposed in the top middle panel.  
 366  
 367  
 368  
 369  
 370  
 371

345 initialized in early spring (doy 105) when the water column is characterized by a relatively  
 346 deep mixed layer ( $\sim 100$  m) and a halocline located between 100 and 150 m (Figure  
 347 2). The forcing by a realistic, positive, net heat flux generates the restratification of  
 348 the water column, with the development of a strong thermocline between 25 and 50 m  
 349 leading to the shoaling of the mixed layer and a subsurface peak in  $N^2$  at about 30 m  
 350 (see Figure 2). A comparison between model outputs and monthly-averaged density  
 351 profiles from underwater gliders collected in June and July over the period 2008-2009  
 352 yields correlation coefficients of  $r = 0.87$  and  $r = 0.88$ , respectively. These high cor-  
 353 relation suggest that *Papa\_summer* numerical experiment captures the vertical spring  
 354 and summer conditions in the Northeast Pacific Ocean.

355 In the horizontal, the prescribed density fronts progressively become unstable  
 356 within the first 60 days of the experiment (Figure 2). During this time, the Total  
 357 Kinetic Energy ( $KE_{tot}$ ) contained in the model domain slowly increases before reach-  
 358 ing a maximum at doy 162, where it remains relatively constant for the rest of the  
 359 simulation. The flattening of the  $KE_{tot}$  curve is used to determine the time necessary  
 360 for the simulation to spin-up, hence determining the start day of the particle-tracking  
 361 experiments. The ocean dynamics associated with *Papa\_summer* are characterized  
 362 using PDFs of horizontal buoyancy gradients ( $M^2 = |\nabla_H b|^2$ ), vertical velocities ( $w$ ),  
 363 and Rossby numbers computed from the normalized vertical component of the relative  
 364 vorticity ( $Ro = (v_x - u_y)/f$  where  $f = 1.12 \times 10^{-4}$ ; Figure 5).

372 Lateral buoyancy gradients in the summer are relatively weak  $\mathcal{O}(10^{-8} \text{ s}^{-2})$  and  
 373 result in low Rossby numbers  $\mathcal{O}(0.1)$ , with positive relative vorticity on the denser  
 374 (north) side of the front and negative relative vorticity on the lighter (south) side

of the front. Corresponding vertical velocities are consistently weaker than 1 m/day ( $<10^{-5}$  m/s) and are characterized by regions of weak upwelling and downwelling on 10 km scales, associated with the meandering of the front (?). Alternating bands of upwelling and downwelling at  $\mathcal{O}(1 \text{ km})$  spatial scale are superimposed, and likely caused by propagating internal waves. Coherent vertical velocity structures extend to depths much greater than the mixed layer depth ( $\sim 25 \text{ m}$ ; Figure 5). The amplitude of the vertical velocity field coincides with the expected order of magnitude given by the scaling  $w \propto Ro f U / N$  (?): using  $Ro \sim 0.1$  (Figure 5),  $N \sim 10^{-2} \text{ s}^{-1}$  (Figure 2),  $f \sim 10^{-5} \text{ s}^{-1}$ , and  $U \sim 0.01 \text{ m/s}$ , we obtain  $w \sim 10^{-6} \text{ m/s}$ , or  $\sim 10^{-1} \text{ m/day}$ .

*Papa-winter* is, on the other hand, initialized in the winter (doy 0) to capture a time period where the mixed layer depth is deeper ( $\sim 100 \text{ m}$ ) and density gradients more pronounced (?). At this time of year, the water column in this region is characterized by the presence of a deep halocline between 100 and 150 m (Figure 3 ?). After spin-up, the vertical stratification remains consistent throughout the model run, and compares well with the vertical profile obtained from glider observations for the month of March ( $r = 0.95$ ; see Figure 3). In the horizontal, prescribed density fronts are much sharper than in summer (i.e., over smaller spatial scales  $\mathcal{O}(1 \text{ km})$  vs.  $\mathcal{O}(10 \text{ km})$ ). Because of these stronger density gradients, combined with the alternating zonal winds and constantly negative surface heat flux, the fronts become unstable more rapidly than in summer (Figure 3). As a result,  $KE_{\text{tot}}$  starts to plateau at doy 48. The experiment is considered spun-up by doy 50 and the particle-tracking experiment is initialized.

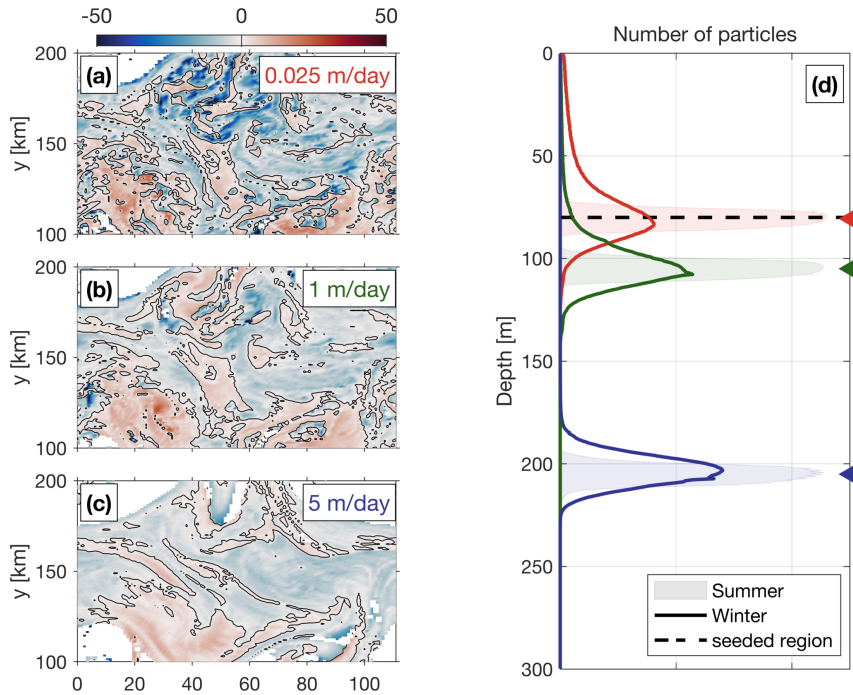
The frontal structures visible in the horizontal buoyancy gradient field are associated with filaments of relatively high Rossby number of  $\mathcal{O}(1)$  (Figure 5). The PDF of relative vorticity reveals a positively-skewed distribution ( $s = 0.68$ ). This is in agreement with the fact that the relative vorticity is more likely to be cyclonic than anticyclonic, based on conservation of potential vorticity (?). Regions with high Rossby number are localized and located in the mixed layer exclusively. In places where the local Rossby number reaches  $\mathcal{O}(1)$ , geostrophic balance is lost and a vertical secondary ageostrophic circulation begins to slump the isopycnals and restore the flow to a more geostrophically-balanced flow. This ageostrophic secondary circulation therefore generates “hot spots” of higher vertical velocities. The fine-scale structures in the vertical velocity field corresponding to  $\mathcal{O}(1)$  Rossby numbers can be seen in Figure 5, with local vertical velocities up to 60 m/day ( $\sim 7 \times 10^{-4} \text{ m/s}$ ). Contrary to the PDF of relative vorticity, the distribution of vertical velocities demonstrate a negative skewness ( $s = -0.25$ ). This is in agreement with the theory: In fact, positive relative vorticity is associated with the dense side of a density front, where vertical velocities are negative (?). Once again, the amplitude of these vertical velocity hot spots is coherent with the scaling  $w \propto Ro f U / N$ : using  $Ro \sim 1$ ,  $N \sim 10^{-2} \text{ 1/s}$ ,  $f \sim 10^{-5} \text{ 1/s}$ , and  $U \sim 0.1 \text{ m/s}$ , we obtain  $w \sim 10^{-4} \text{ m/s}$ , or  $\sim 10^1 \text{ m/day}$ .

Comparing *Papa-summer* and *Papa-winter* highlights the different dynamical regimes in the two experiments. In *Papa-winter*, density fronts tend to be sharper, meaning larger density gradients over shorter spatial scales. When computed at the kilometer-scale, the PDF of horizontal buoyancy gradients in *Papa-winter* exhibits a longer tail than in *Papa-summer* (Figure 5). When compared to observations, the PDFs of  $M^2$  in *Papa-summer* and *Papa-winter* demonstrate a correlation with observations of  $r = 0.93$  and  $r = 0.95$ , respectively.

The wider PDF of vertical velocities in *Papa-winter* shows advective velocities that match and exceed typical gravitational sinking velocities, particularly for smaller, and therefore slower-sinking, particulate organic material. The secondary ageostrophic circulation that develops at submeso-scales (i.e.,  $Ro \mathcal{O}(1)$ ) therefore generates an export mechanism that directly competes with the traditional paradigm that relies on gravitational sinking leading the export of particulate matter in the ocean.

### 428 3.2 Gravitational and Advective Export of POC

429 Both model experiments described above were then used to investigate the re-  
 430 lationship between ocean dynamics and particle downward flux, using Lagrangian  
 431 particle-tracking. Domain-averaged, downward particle flux is expected to be a com-  
 432 bination of the flux driving by gravitational sinking ( $\langle w_s B \rangle$ ), and by the vertical ad-  
 433 vective currents affecting the particle along its pathway ( $\langle wB \rangle$ ). The deviation in  
 434 particle depths from the traditional one-dimensional gravitationally driven model is  
 435 shown in Figure 6 for both summer and winter cases. In the summer, the PDF of par-  
 436 ticle density versus depth remains relatively narrow through time, and is centered on  
 437 a depth level that can be predicted using a simple 1D gravitational model (see shaded  
 438 curves in Figure 6). The spread in the particle density also vary little among particle  
 439 classes with different sinking velocities, suggesting that downward fluxes of particles  
 440 is greatly dominated by gravitational settling and is not subject to significant vertical  
 441 ocean currents.



442 **Figure 6.** [left] The median depth anomaly of particles with a sinking speed (a) 0.025 m/d,  
 443 (b) 1 m/d, (c) 5 m/d within each grid cell for the winter case 25 days after particles are released.  
 444 The ‘depth anomaly’ is with respect to the ‘expected’ sinking depth (= sinking speed  $\times$  time  
 445 since release). Blue (red) grid cells indicate that the median depth of particles in this cell is  
 446 deeper (shallower) than expected, based on a 1D gravitational model where  $z = w_s \times t$ . [right] (d)  
 447 Probability Distribution Function (PDF) of particles as a function of depth for each velocity class  
 448 (red = 0.025 m/day; green = 1 m/day; blue = 5 m/day). The winter distribution is shown as  
 449 thick lines, while the summer distribution is represented by the shaded regions. Triangle markers  
 450 indicate the expected depth of particles after 25 days based on the 1D gravitational model, which  
 451 is used as a reference to compute the depth anomalies. Release depth is indicated by the thick  
 452 dashed line.

453 In the winter, however, PDFs of particle density versus depth is wider, in agree-  
 454 ment with the stronger vertical ocean currents occurring in the winter (see Figure 5).

455 A top-view of the deviation in the downward particle flux from the traditionally con-  
 456 sidered 1D gravitational model can be seen in Figure 6 (panels (a)-(c)). Slower-sinking  
 457 particles deviate more than faster-sinking particles, exhibiting median depth anom-  
 458 alies up to 50 m. This is due to the fact that slower-sinking particles spend more time  
 459 in the mixed layer, where most of the stronger vertical currents tend to occur (Figure  
 460 5). An interesting result emerges from the spatial distribution of the depth-anomaly:  
 461 both positive (i.e., particles are shallower than expected) and negative (i.e., particles  
 462 are deeper than expected) anomalies are organized into features with a length-scale  
 463  $\mathcal{O}(1\text{-}10 \text{ km})$ . This further highlights the importance of winter submesoscale circulation  
 464 for vertical fluxes of particles.

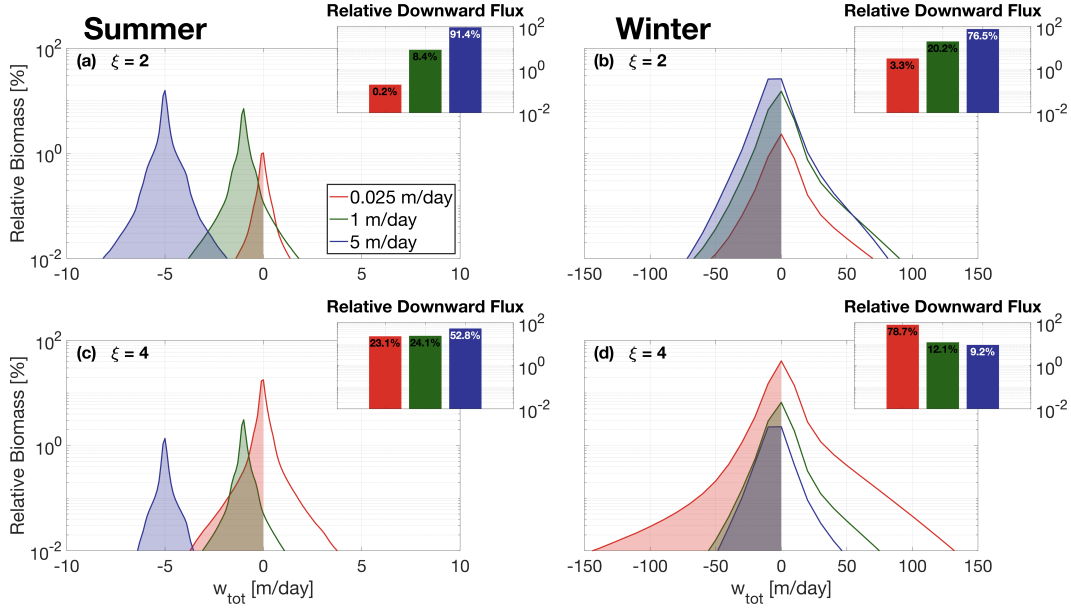
465 A relative amount of biomass is associated to the particles using Equation (8).  
 466 PDFs of relative biomass as a function of the vertical velocity is shown in Figure 7.  
 467 Following the traditional paradigm derived from the simple 1D gravitational model, the  
 468 downward flux of biomass in the summer is dominated by faster-sinking particle classes  
 469 capable of carrying particulate material downwards more efficiently. The contribution  
 470 of slower-sinking particles, however, depends critically on the slope of the size spectrum  
 471 (see Figure 4). As the Junge slope increases, the spectrum of biomass steepens, and  
 472 the relative contribution of slower-sinking particles to the downward biomass flux  
 473 significantly increases (Figure 7c). In fact, the contribution of slower-sinking particles  
 474 to the summer downward flux increases by a factor 100 (from 0.2% to 20%) when the  
 475 Junge slope varies from  $\xi = 2$  to  $\xi = 4$ . While significant, the impact of a change in  
 476 the Junge slope in summer conditions does not challenge the dominant role played by  
 477 faster-sinking particles. This result can be explained by the fact that, in the summer,  
 478 vertical velocities are weak and vertical biomass fluxes are therefore gravitationally-  
 479 driven ( $\langle w_s B \rangle > \langle w B \rangle$ ).

487 In the winter, PDFs of relative biomass as a function of vertical velocities present  
 488 a much larger spread, with velocity magnitudes exceeding 50 m/day. For  $\xi = 2$ ,  
 489 the relative contribution of slower-sinking particles to the downward flux significantly  
 490 increases from 0.2% in the summer to about 3% in the winter, demonstrating the  
 491 impact advective velocities alone can have on vertical fluxes (Figure 7b). Nevertheless,  
 492 slower-sinking particles remain a relatively small contributor to the total downward  
 493 flux of biomass. When winter ocean dynamics are coupled with a steeper Junge slope,  
 494 however, slower-sinking particles largely dominate the downward biomass flux. In  
 495 our winter simulations with  $\xi = 4$ , we find that the slowest-sinking particle class is  
 496 responsible for about 79% of the biomass flux (Figure 7d).

497 Our results show that both a steepening of the particle size spectrum and the  
 498 presence of submesoscale dynamics can enhance the contribution of slower-sinking par-  
 499 ticles to the downward biomass flux. While the former is simply due to an increase in  
 500 particle density in slower-sinking particle classes, the latter is attributed to the larger  
 501 vertical velocity generated by submesoscale instabilities. When both are combined,  
 502 as expected in the wintertime, slower-sinking particles then become the leading con-  
 503 tributor to the downward biomass transport. However, slower-sinking particles are  
 504 generally expected to remineralize on timescales shorter than their export timescale,  
 505 fueling the argument that the focus should be upon faster-sinking particle classes. The  
 506 impacts of remineralization on export are thus considered in the following section to  
 507 test the robustness of the findings.

### 508 3.3 Particle Remineralization

509 Both submesoscale dynamics and the Junge slope were identified as key factors  
 510 impacting the respective role played by different particle classes in driving downward  
 511 biomass fluxes. Simple Lagrangian particles were used to isolate the effects of these  
 512 two factors. In reality, however, sinking velocities of particulate matter varies in time

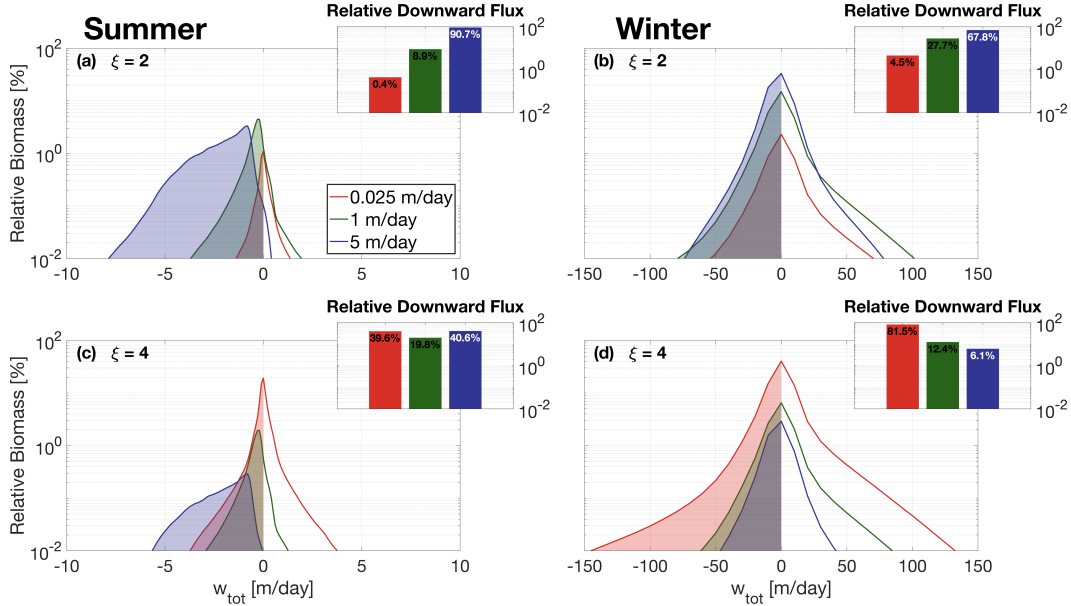


480 **Figure 7.** Probability Distribution Function (PDF) of relative biomass versus total vertical  
 481 velocity (sinking + advective) along particle trajectories in the summer case [left] and winter case  
 482 [right], with a Junge slope of 2 [top] and 4 [bottom]. PDFs are computed from the whole 24-day  
 483 particle tracking experiments. Inserts show the integrated relative downward biomass flux asso-  
 484 ciated with each sinking-velocity class, categorized according to their initial sinking velocity (red  
 485 = 0.025 m/day; green = 1 m/day; blue = 5 m/day). Both winter dynamics and steeper Junge  
 486 slopes tend to increase the relative contribution of slower-sinking particles.

513 as the particles slowly remineralize. A remineralizing behavior was therefore imple-  
 514 mented for the Lagrangian particles, using Equation (10), to investigate the impact  
 515 that remineralization processes have on our findings. The traditional paradigm relies  
 516 on the fact that slow-sinking particles tend to fully remineralize over short timescales,  
 517 further enhancing the importance of faster-sinking particles classes in driving down-  
 518 ward biomass fluxes. While this paradigm holds for flatter Junge slope, where the  
 519 biomass content is dominated by faster-sinking particles, it becomes unfit at steeper  
 520 slopes.

521 Figure 8 compares the relative biomass and downward biomass fluxes associated  
 522 with each of the modeled particle classes for  $\xi = 2$  and  $\xi = 4$  including the remineral-  
 523 ization scheme. As previously detailed, downward fluxes of biomass are dominated by  
 524 faster-sinking particles during summertime and in the absence of remineralization (see  
 525 Figure 7). This is due to the fact that the flux of biomass  $\langle w_{tot}B \rangle = \langle w_s B \rangle + \langle w B \rangle$   
 526 is driven by  $\langle w_s B \rangle$ , despite a smaller relative biomass content per particle. This is  
 527 characteristic of a gravitationally-driven system, where settling velocity dictates the  
 528 contribution to downward fluxes. Implementing remineralization processes, however,  
 529 directly affects the particle settling velocity which slows down as particles remineralize.  
 530 This effect can particularly be seen in Figure 8a and c, where PDFs of relative biomass  
 531 per particle class are shifted towards weaker vertical velocities than in the absence of  
 532 remineralization, as predicted by Equation (10).

533 In an advectively-driven system where  $\langle w_s B \rangle \sim \langle w B \rangle$ , the relative amount of  
 534 biomass content in a particle class becomes important and dictates the respective con-  
 535 tribution of each particle class to the total downward biomass fluxes. This shift from a



533 **Figure 8.** Same as Figure 7, but including particle remineralization (see Equation 10).

537 gravitationally-driven to an advectively-driven system is observed when implementing  
 538 particle remineralization in the summer (Figure 8): in the absence of remineralization,  
 539 faster-sinking particles dominate the downward biomass fluxes (53%; see Figure 7c).  
 540 When remineralization processes are considered, slower-sinking particles contribute  
 541 more to biomass fluxes (see inset in Figure 8c). As shown in Figure 7, downward  
 542 biomass fluxes in the wintertime are generally advectively-driven, due to the larger  
 543 vertical velocities associated with wintertime ocean dynamics. Biomass fluxes are  
 544 dominated by the slower-sinking particles when  $\xi = 4$ , representing 79% of the down-  
 545 ward biomass flux (Figure 7d). Even after implementing the remineralization scheme,  
 546 slower-sinking particles remain the largest contributor to downward biomass fluxes  
 547 (82%; see Figure 8d).

548 These results highlight the importance in considering slower-sinking particle  
 549 classes when considering downward biomass fluxes. It also demonstrates that, con-  
 550 trarily to the traditional paradigm, remineralization processes enhance the role played  
 551 by slower-sinking particles in biomass fluxes, in cases where the biomass spectrum  
 552 slope is negative.

## 553 4 Discussion

### 554 4.1 Dynamical Regimes

555 *Papa-summer* and *Papa-winter* experiments were designed to statistically cap-  
 556 ture the ocean dynamics at Station Papa ( $145^{\circ}\text{W}$ ,  $50^{\circ}\text{N}$ ) in the Northeast Pacific  
 557 Ocean. After spin-up, the model demonstrated similar distributions of both horizontal  
 558 ( $M^2$ ) and vertical ( $N^2$ ) density gradients to observational estimates from underwater  
 559 gliders (see Figures 2, 3, and 5). The two experiments, however, show significantly  
 560 different distributions of  $M^2$ , with the winter distribution exhibiting a longer tail, due  
 561 to sharper density gradients. The tail of the wintertime distribution is only partially  
 562 captured by the glider data, due to the fact that underwater gliders sampled gradients  
 563 at spatial scales of 10 km and greater, while the model has a horizontal resolution of  
 564 500 m, allowing sharper submesoscale fronts and filaments to be formed.

Studies investigating submesoscale dynamics traditionally focused on regions where the presence of submesoscale fronts and filaments are established, such as western boundary currents with strong gradients (?, ?, ?), or the edge of mesoscale features (?, ?, ?). The seasonality in submesoscale dynamics captured in the glider dataset at Station Papa and reflected in the model experiments, echoes the behavior seen from recent observational studies conducted at a similar latitude in the Atlantic Ocean, which demonstrate the intensification of submesoscale dynamics in the wintertime (?, ?, ?). Despite being sometimes qualified as an “eddy desert” with low kinetic energy (?, ?), ocean characteristics in the eastern part of the Pacific subpolar gyre suggest the presence of submesoscale features in the wintertime: strong density gradients, localized Rossby numbers of order 1, a balanced Richardson number  $Ri_b = \frac{f^2 N^2}{M^4}$  smaller than 1, a positively skewed distribution in vorticity, and a negatively skewed distribution of vertical velocities (see Figure 5; ?, ?, ?, ?).

Strong downward velocities are hypothesized to enhance POC export by advecting slower-sinking particles out of the mixed layer. *Papa\_winter* indeed exhibits vertical velocities more than 20 times larger than in *Papa\_summer*. The vertical currents in *Papa\_winter*, however, tend to be much patchier than the weaker vertical currents observed in *Papa\_summer*. Because both particle production and downward vertical velocities present a high degree of patchiness, it requires a certain level of covariance between the two fields for the export to effectively be enhanced (?, ?). A more realistic seeding strategy for Lagrangian particles, such as one guided by biological tracers, would likely provide important information towards a better understanding of the effects of patchiness on POC export at submeso-scales

The hypothesis tested in this study is that submesoscale activity enhances export of particulate matter at Station Papa by shortening the export timescale of particulate matter. The wintertime intensification in submesoscale activity has the potential to indeed enhance export (see discussion in Section 4.2). However, the seasonal cycle in submesoscale activity is out of phase with the one in net community productivity, which peaks in the spring and summertime when the mixed layer is shallower (?, ?). Two mechanisms are therefore present to potentially sustain a year-long POC export flux: In the winter, less particulate material is present in the mixed layer, but active submesoscale dynamics tend to enhance the POC export flux by advecting the more numerous slower-sinking particles into the ocean interior. In the summer, the production of POC is at its yearly maximum, but export tends to be dominated by gravitational sinking, which favors faster-sinking particles and thus exclude part of the particle spectrum from contributing to the export flux.

## 4.2 Downward Fluxes

Analyses of particle tracking experiments reveal that the contribution of slower-sinking particles to the downward particulate flux depends on two main factors: (1) the dynamics of the oceanic flow field, and (2) the slope of the size spectrum (i.e., the Junge slope  $\xi$ ).

Mixed layer ocean dynamics at station Papa change significantly between the winter and the summer. In the winter, submesoscale dynamics are intensified, and sharp fronts and filaments develop in the mixed layer. This seasonal change in dynamics is consistent with recent observations (?, ?, ?), and models (?, ?, ?, ?) characterizing the seasonal cycle of submesoscale dynamics. The winter intensification in submesoscale dynamics was proven to have an important impact on the downward flux of all sinking-velocity classes modeled in this experiment.

In the summer, gravitational sinking governs a downward particulate flux, which is dominated by faster-sinking particles, with little to no contribution from slower-sinking particles. In the winter, however, vertical fluxes tend to be advectively-driven,

which leads to a slightly weaker downward flux of faster-sinking particles than in the summer due to resuspension, but a much larger flux of slower-sinking particles, which are present in far greater numbers (Figure 7). The gravitationally-driven flux in the summer is mechanistically different from the advectively-driven winter flux, which raises the question as to which process is most efficient in driving a downward flux of particulate material.

In the absence of remineralization, both a steeper size spectrum slope ( $\xi > 3$  in this case) and enhanced submesoscale dynamics, increase the contribution of slower-sinking particle classes to the downward biomass flux. This is only when both of these conditions are combined, however, that slower-sinking particles dominate the downward flux of biomass (Figure 7). This is a significant result, as Junge slopes greater than 3 have been observed in the ocean: In-situ observations yield average spectral slopes varying between 3.5 and 4.5 (see Table 2 in ?, ?), while spectral analysis of satellite data suggest global spectral slopes varying between 3 and 6. More recent observational work located in the Northeast Pacific, including Station Papa, found a spectral slope also greater than 3 (? , ? , ?). Junge slopes are expected to vary in space, depending on the community composition, both lateraly and vertically (? , ? , ?), as well as in time; spectrum slopes tend to be flatter during a spring bloom event, where larger particles (e.g., diatoms) are produced in large quantities, and steeper during the wintertime, when communities are mostly composed of small particles (? , ? , ? , ?). The threshold value of  $\xi = 3$  for a change in the biomass spectral slope (see Figure 4b) is of course a consequence of first-order approximations used in this study describing the relationships between particle size, sinking velocity, and biomass content. Nevertheless, our results demonstrate the importance of including the smaller particle size range of the particle spectrum, in the estimation or measurement of vertical fluxes, especially when submesoscale dynamics are active. It also highlights the importance of better constraining the relationships linking particle size, sinking velocity, and biomass content.

Introducing remineralization processes significantly decreases the biomass flux. Counter-intuitively, however, the implementation of a remineralization scheme further strengthens the contribution of slower-sinking particles to the biomass flux<sup>c1</sup>, once particles have left the euphotic layer (Figure 8). This can be explained by the fact that remineralization processes have a greater impact on sinking-velocity classes that rely on gravitational sinking to be exported, as these particles decelerate as they remineralize. In the summer, all particle classes are similarly affected by remineralization, as downward fluxes are gravitationally-driven. In the winter, however, slower-sinking particles are exported through advective processes. Their export timescale is barely affected by remineralization processes as it only depends on local ocean dynamics. <sup>c2</sup>Changing the remineralization timescale would therefore only affect the results in a gravitationally-driven flux: increasing the timescales (i.e. slower remineralization) would give more weight to the smaller classes, while decreasing the timescales (i.e. faster remineralization) would favor faster sinking particles to drive the downward flux. In an advectively-driven flux, however, all particles classes are equally affected by remineralization (i.e. lose 12% of their biomass per day). While this affects the total amount of biomass flux, it does not impact the respective contributions of the different particle classes to the downward biomass flux.

These results are robust to the range of sinking rates explored. If one considers a particle class with a sinking rate far exceeding the vertical advective velocity (e.g., 100 m/day; ?, ?), then the associated biomass flux can be estimated by relying on the traditional 1-D paradigm, assuming  $w_{tot} \approx w_s$ . Combining this approximation

---

<sup>c1</sup> *Text added.*

<sup>c2</sup> *Text added.*

with Equation 8 shows that the slope of the biomass flux spectrum is positive for  $\xi < 5$ , in which case very fast-sinking particles would dominate vertical biomass fluxes. However, for  $\xi > 5$ , the slope of the biomass flux spectrum becomes negative as well, meaning that the biomass flux is always dominated by the slow-sinking particle classes, regardless of the ocean dynamical regime. <sup>c3</sup>While values of  $\xi > 5$  have been estimated by ? (?) <sup>c4</sup>using satellite data, in-situ estimated values of  $\xi$  tend to range between 2 and 4.5(?, ?, ?).

The results of this study suggest that slow- and non-sinking particles must be considered when studying the downward flux of particulate matter in the upper ocean. The patchiness associated with both particle production and submesoscale features poses a real observational challenge to properly resolve vertical fluxes. Based on our findings, subsequent studies should focus on testing the impact of patchiness on vertical fluxes. In the wintertime, when size spectral slope is steep and submesoscale dynamics most active, vertical fluxes could be grossly underestimated depending on the level of co-occurrence between particle production and stronger vertical currents.

## 5 Conclusion

The main conclusions of this study are:

1. Ocean dynamics in the subpolar Northeast Pacific exhibit a seasonal cycle with low submesoscale activity in the summertime, and more submesoscale features present in the wintertime. Submesoscale dynamics generate larger, and asymmetric, vertical currents leading to a vertical biomass flux driven by advective processes, as opposed to gravitational sinking in the summertime.
2. Submesoscale dynamics generally enhance the downward particulate flux by increasing the contribution of slower-sinking particles to the total flux through advective transport. The slower-sinking particles are found to be significant for export, and can be even make the dominant contribution under certain conditions.
3. The contribution of slower-sinking particles to the downward biomass flux depends on the slope of the particle size spectra (i.e., the Junge Slope), that controls the relative number of particles per size class. Two cases emerge from this study:
  - (a) If the Junge slope is smaller than 3, larger particles contribute most to vertical biomass fluxes independently of flow dynamics, as there are no mechanisms capable of selectively advecting slower-sinking particles. The system is described as gravitationally-driven.
  - (b) If the Junge slope is greater than 3, as most commonly observed, ocean dynamics become key for determining which particle classes dominate the downward flux. As submesoscale dynamics become more active, ageostrophic circulations leading to larger vertical velocities develop. In these conditions, downward biomass fluxes are largely driven by the slower-sinking particle classes.
4. Remineralization processes <sup>c1</sup>below the euphotic depth logically reduce the amount of biomass flux. However, it unexpectedly enhances the role of slower-sinking particles, which are advectively transported. The impact of remineralization

<sup>c3</sup> While considered large, values of  $\xi > 5$  remain realistic and fall within the range obtained from satellite-based estimates

<sup>c4</sup> Text added.

<sup>c1</sup> Text added.

710       <sup>c2</sup>below the euphotic depth is greater on faster-sinking particles since it affects  
 711       both the biomass content and their sinking velocity.

712       **Acknowledgments**

713       The work was funded by NASA grant NNX16AR48G, to complement the EX-  
 714       port Processes in the global Ocean from RemoTe Sensing (EXPORTS) program. We  
 715       would like to thank A. Thompson (Caltech) for his useful comments and sugges-  
 716       tions, N. Pelland (NOAA) and C. Eriksen (University of Washington) for sharing  
 717       the glider data collected at Ocean Station Papa, as well as S. Essink for his assistance  
 718       in developing the particle-tracking code. All data used in this manuscript are pub-  
 719       licly available: Ocean Station Papa data is available on PMEL's website (<https://www.pmel.noaa.gov/ocs/Papa>; ?, ?) and gridded Argo products can be downloaded  
 720       at <http://www.seanoe.org/data/00348/45945> (? , ?). Glider data is archived at  
 721       the University of Washington's Library (<http://hdl.handle.net/1773/41656>; ?, ?).  
 722       Code to reproduce analysis and figures are publicly available at <https://github.com/>  
 723       `matdever/Size-differentiated_Export_GBC` (? , ?). Due to the very large filesize,  
 724       model outputs and particle trajectories are available on request.  
 725

726       **References**

727       Alkire, M., D'Asaro, E., Lee, C., Perry, M., Gray, A., Cetinic, I., ... González-  
 728       Posada, A. (2012). Estimates of net community production and export using  
 729       high-resolution, Lagrangian measurements of O<sub>2</sub>, NO<sub>3</sub><sup>-</sup>, and POC through the  
 730       evolution of a spring diatom bloom in the North Atlantic.

---

<sup>c2</sup> *Text added.*